BOREAL ENVIRONMENT RESEARCH 19 (suppl. B): 215–236 © 2014
ISSN 1239-6095 (print) ISSN 1797-2469 (online) Helsinki 30 September 2014

Methods for determining particle size distribution and growth rates between 1 and 3 nm using the Particle Size Magnifier

Katrianne Lehtipalo[1,2,*], Johannes Leppä[3], Jenni Kontkanen[1], Juha Kangasluoma[1], Alessandro Franchin[1], Daniela Wimmer[1], Siegfried Schobesberger[1], Heikki Junninen[1], Tuukka Petäjä[1], Mikko Sipilä[1], Jyri Mikkilä[2], Joonas Vanhanen[2], Douglas R. Worsnop[1,4] and Markku Kulmala[1]

[1)] *Department of Physics, P.O. Box 64, FI-00014 University of Helsinki, Finland (*corresponding author's e-mail: katrianne.lehtipalo@helsinki.fi)*
[2)] *Airmodus Oy, Pietari Kalmin katu 1 F 1, FI-00560 Helsinki, Finland*
[3)] *Finnish Meteorological Institute, Atmospheric Composition Research, P.O. Box 503, 00101 Helsinki, Finland*
[4)] *Aerodyne Research Inc., 45 Manning Road Billerica, MA 01821-3976, USA*

Received 30 Oct. 2013, final version received 21 Feb. 2014, accepted 3 Mar. 2014

Lehtipalo, K., Leppä, J., Kontkanen, J., Kangasluoma, J., Franchin, A., Wimmer, D., Schobesberger, S., Junninen, H., Petäjä, T., Sipilä, M., Mikkilä, J., Vanhanen, J., Worsnop, D. R. & Kulmala, M. 2014: Methods for determining particle size distribution and growth rates between 1 and 3 nm using the Particle Size Magnifier. *Boreal Env. Res.* 19 (suppl. B): 215–236.

The most important parameters describing the atmospheric new particle formation process are the particle formation and growth rates. These together determine the amount of cloud condensation nuclei attributed to secondary particle formation. Due to difficulties in detecting small neutral particles, it has previously not been possible to derive these directly from measurements in the size range below about 3 nm. The Airmodus Particle Size Magnifier has been used at the SMEAR II station in Hyytiälä, southern Finland, and during nucleation experiments in the CLOUD chamber at CERN for measuring particles as small as about 1 nm in mobility diameter. We developed several methods to determine the particle size distribution and growth rates in the size range of 1–3 nm from these data sets. Here we introduce the appearance-time method for calculating initial growth rates. The validity of the method was tested by simulations with the Ion-UHMA aerosol dynamic model.

Introduction

Studying processes in which new aerosol particles are formed via gas-to-particle conversion requires measurements also in the size range 1–2 nm, i.e. exactly at the size of the nucleating clusters (Kulmala *et al*. 2013). New particle formation happens frequently in the atmosphere in many different kinds of environments (e.g. Kulmala *et al*. 2004, Manninen *et al*. 2011), but also in some industrial processes and in engine exhausts (e.g. Lähde *et al*. 2009). One of the reasons why the molecular level processes leading to new particle formation are not yet completely understood has been the inability to detect neutral particles below 3 nm in diameter.

The need to measure smaller particles has led to a rapid development of new measurement

Editor in charge of this article: Hannele Korhonen

techniques for detecting nucleating particles (Kulmala *et al*. 2012). Ion spectrometers like the Balanced Scanning Mobility Analyzer (BSMA; Tammet 2006) and Neutral Cluster and Air Ion Spectrometer (NAIS, Mirme *et al*. 2007) can be used to measure ions down to 0.8 nm in mobility diameter, and NAIS can additionally detect neutral particles down to ~2 nm (Asmi *et al*. 2009). Iida *et al*. (2009) showed that diethylene glycol (DEG) has preferable characteristics for activating small particles, and several Condensation Particle Counter (CPC) applications using DEG as condensing fluid have been developed (Jiang *et al*. 2011, Vanhanen *et al*. 2011, Kuang *et al*. 2012a). Recently Wimmer *et al*. (2013) characterized the performance of a Particle Size Magnifier (PSM; Airmodus A09) and laminar flow type DEG-CPC (modified TSI 3776) and showed that they can be used to detect particles even close to 1 nm in mobility diameter.

A CPC measures the total particle number concentration. For obtaining a size distribution, one normally needs to combine it with a charger and a size-selection method, for instance a differential mobility analyzer (DMA). Unfortunately, the charging efficiency of particles smaller than 3 nm is very low (Hoppel and Frick 1986, Wiedensohler 1988), and DMAs often have substantial losses for the smallest particles, leading to very poor counting efficiencies below 3 nm. Therefore, most size spectrometers, like the Differential or Scanning Mobility Particle Sizer (DMPS/SMPS; Flagan 1998), are normally used to measure only at sizes larger than 3 nm, and large deviations between individual instruments exist below 10 nm (Wiedensohler *et al*. 2012). Jiang *et al*. (2011) developed recently a DEG-SMPS reaching also smaller sizes, and neutral clusters have been measured with a cluster-CIMS (Zhao *et al*. 2011). Size distributions have also been obtained using a pulse-height CPC (Sipilä *et al*. 2009, Lehtipalo *et al*. 2009, 2010), in which the supersaturation profile inside the CPC condenser is used to determine the size distribution between 1.5–5 nm. However, size distribution data sets reaching the smallest particles are still sparse, and they are difficult to compare due to differences in methods, instruments and their size ranges.

There are only few studies addressing the initial growth rate (GR) of particles. The NAIS and BSMA have been used to study the growth of 1.5–3 nm ions during field measurements (Hirsikko *et al*. 2005, Yli-Juuti *et al*. 2011). However, ion spectrometers are not suitable for measuring the growth of sub-2 nm neutral particles. The initial particle growth rates have been studied by using the size distribution data from the DEG-SMPS and solving the GR from the general dynamic equation (Kuang *et al*. 2012b). Alternatively, the GRs from 1–3 nm have been estimated from the time lag between rise in sulphuric acid concentration and the start of a nucleation event detected at 3 nm (e.g. Sihto *et al*. 2006), or the time lag between CPCs at different cut-off sizes (Riccobono *et al*. 2012). Modelling studies and data evaluation have shown that especially at the beginning of the growth process, the esimated GR values can be very sensitive to the method used for determining the growth rate (Leppä *et al*. 2011, Yli-Juuti *et al*. 2011, Riccobono *et al*. 2012).

Here we describe several methods to obtain the size distribution of particles below 3 nm from the PSM data, introduce the appearance time method to calculate the growth rate of sub-3 nm particles, compare their outcomes with the size distributions and GRs obtained using other instruments, and validate the appearance time method by simulations. So far some of those methods were used in field measurements inside the boreal forest at the Hyytiälä SMEAR II station (Kulmala *et al*. 2013) and in the CLOUD nucleation experiments at CERN (Kirkby *et al*. 2011, Almeida *et al*. 2013). In the CLOUD experiments it was demonstrated that the PSM can detect particles sooner after the initiation of the particle formation process than any other particle counter used, and that the data is comparable to cluster distributions measured with mass spectrometers (Schobesberger *et al*. 2013).

Determining the particle size distribution

The Particle Size Magnifier

The Particle Size Magnifier (Airmodus A09/A10; *see* Fig. 1) is a pre-conditioner for a CPC, using diethylene glycol for activating and grow-

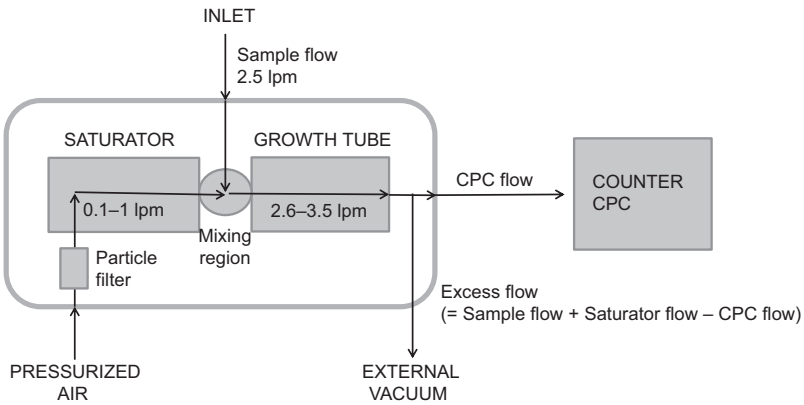

Fig. 1. A flow diagram of the Particle Size Magnifier showing the saturator, in which clean air is saturated with DEG, the mixing region, in which the saturated air is mixed with the sample air from the inlet, and the growth tube, in which DEG condenses on the particles. After the growth tube a part of the flow is discarded and a part of it is directed to the CPC.

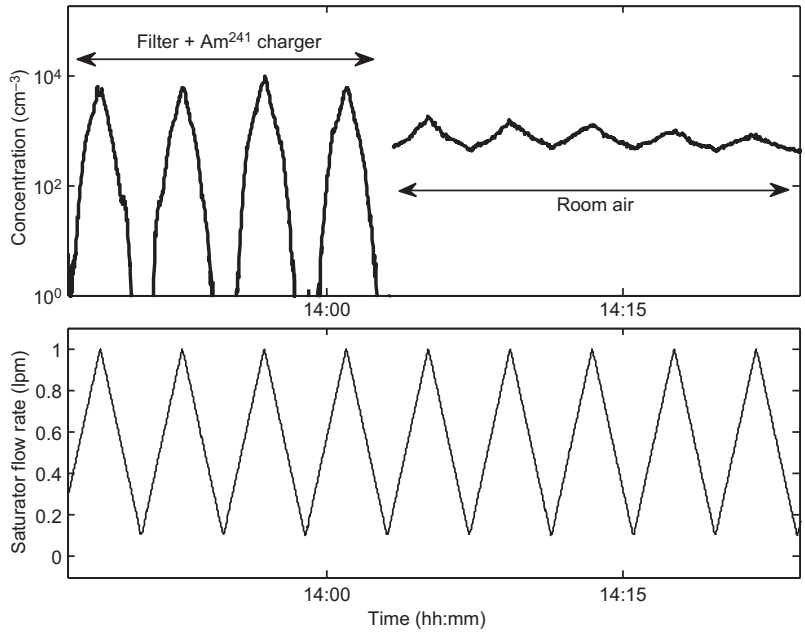

Fig. 2. Example of the scanning mode in the PSM. The saturator flow rate is changed continuously between 0.1–1 lpm in 120 s. The upper panel gives the total particle concentration between ~1.5 nm–1 μm measured either through a particle filter and a radioactive charger or directly from room air, and the lower panel gives the saturator flow rate.

ing the sample aerosol particles until the smaller particles are about 90 nm in diameter. In this study, further growth to detectable sizes, and particle optical counting was done with the butanol CPC (TSI 3010/3772), but in principle any CPC type can be used as the second stage after the PSM. Details of the instrument are presented by Vanhanen *et al*. (2011).

The diethylene glycol supersaturation inside the PSM, which primarily defines the lowest particle size that can be measured, is created by turbulently mixing heated saturated air with the cooler sample air. The achieved level of supersaturation can be changed by changing the mixing ratio of the sample and saturator air. In practice, this is done by changing the flow rate through the saturator. Thus the cut-off size of the instrument can be varied by scanning the saturator flow rate. Compared with a laminar flow type CPC, in which the supersaturation is controlled only by temperature differences, the mixing type design enables changing the supersaturation much faster, and thus getting size information of the particles with a reasonable time resolution.

For scanning the PSM cut-off size, we used a cycle of 120 steps between saturator flow rates of 0.1 and 1 liters per minute (lpm) within 120 s (equaling to an increase/decrease of 0.0075 lpm s^{-1}). The scanning time was chosen so that the change is slow enough to ensure stable flow rates. An example of the PSM raw data measured in the scan mode is given in Fig. 2. Here,

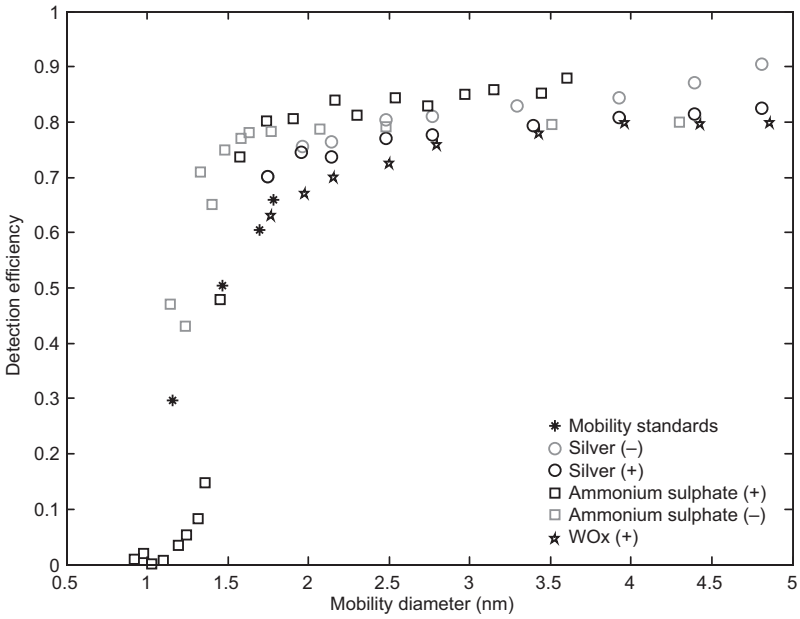

Fig. 3. Total detection efficiency at the highest mixing ratio (f_{sat} = 1 lpm) of PSM for positively- (+) and negatively-charged (–) test particles of different compositions.

we first measured filtered particle-free air which was going through a radioactive source (^{241}Am), which produces a high concentration of ions smaller than about 1.5 nm in mobility diameter (Steiner and Reischl 2012). The concentration shown by the PSM was about zero with the lowest saturator flow rates (f_{sat} < 0.3 lpm), but the concentration rose rapidly as the saturator flow rate was increasing and the ions produced in the charger were activated. After the charger test, we measured room air in the laboratory. Now the total concentration remained above 5×10^2 cm^{-3} at all saturator flow rates, as the larger particles activate already at the lowest mixing ratios. However, a distinct scan cycle is still visible, indicating the presence of 1–3 nm particles in the room air.

Calibration

Laboratory calibrations were done to characterize the detection efficiency of the PSM-CPC system for particles of different size and composition, and to establish a relation between the flow mixing ratio and the activation size, which was needed for extracting a size distribution and finally a growth rate of the particles from the raw data.

We produced ammonium sulphate and silver clusters and particles in a tube furnace (nucleation-condensation technique). The aerosol was charged with an ^{241}Am charger. Particles with a certain mobility size were selected with a high-resolution Herrmann DMA (Herrmann *et al*. 2000). In case of the ammonium sulphate calibrations, the composition of the produced particles and the cleanliness of the sample were verified with a high-resolution mass spectrometer (APi-TOF; Junninen *et al*. 2010). The reference instrument for concentration in the calibrations was a TSI 3068B electrometer. The other test aerosols were tungsten oxide particles from a Grimm WOx generator, and mobility standards (Ude and Fernandez de la Mora 2005) produced by electrospraying. The calibration setup and mass/mobility spectra of the measured ions are presented in Kangasluoma *et al*. (2013).

The total detection efficiency as a function of size for different test particles in the PSM at the highest mixing ratio (f_{sat} = 1 lpm) is shown in Fig. 3. The cut-off size (50% detection efficiency) was 1.2–1.5 nm depending on the particle composition. These results are similar to the ones presented in earlier studies (Vanhanen *et al*. 2011, Kangasluoma *et al*. 2013, Wimmer *et al*. 2013). Activation of the differently-sized ammonium sulphate particles as a function of the

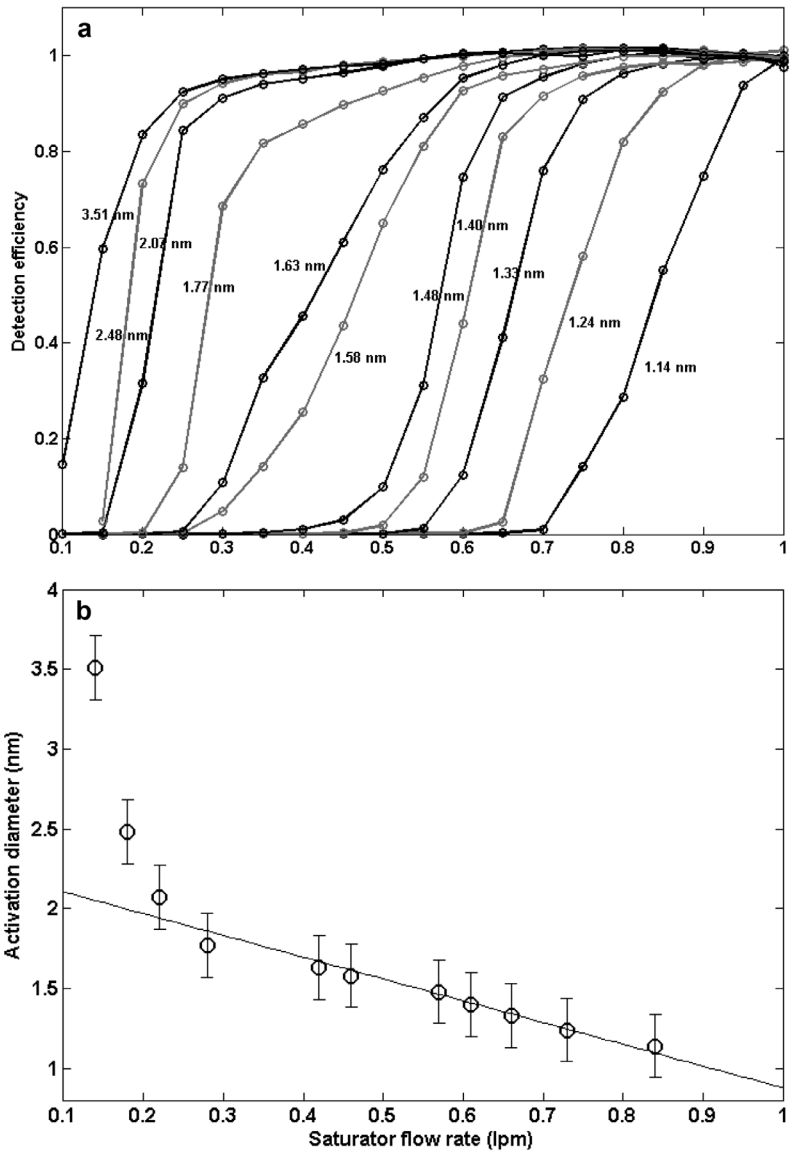

Fig. 4. Detection efficiency of differently-sized negatively-charged ammonium sulphate clusters and particles in the PSM (normalized to 1) as (**a**) a function of saturator flow rate, and (**b**) their size as a function of saturator flow rate at which 50% of them were activated. The line is a linear fit between 0.2–1 lpm, which is the range used in the data inversion. Due to the effect of particle composition on the activation, an error of ± 0.2 nm (bars) was assumed (Kulmala *et al.* 2012).

saturator flow rate is illustrated in Fig. 4. Here, the data is scaled to one to account for the lower total detection efficiency at the smaller sizes due to diffusional losses of particles inside the PSM and/or the CPC (TSI 3010). Thus, it gives the activation efficiency of particles, i.e. the 50% value gives the saturator flow rate at which half of the particles of that size are activated (activation diameter). It can be seen (Fig. 4b) that in the size range from 1 to 2 nm (0.2 lpm < f_{sat} < 1 lpm) the relation between the saturator flow rate and the activation diameter is almost linear. The activation curves of particles in the PSM are clearly steeper than in laminar flow DEG-CPCs, mainly due to lower losses of small particles (Wimmer *et al*. 2013), and we see that it can clearly distinguish particles with 0.1 nm difference in diameter.

The effect of sample particle composition on their activation probability is discussed in Kangasluoma *et al*. (2013, 2014), hence here we only state that the overall composition effect on the activation diameter is in the order of ±0.2 nm for inorganic samples (Kulmala *et al*. 2012).

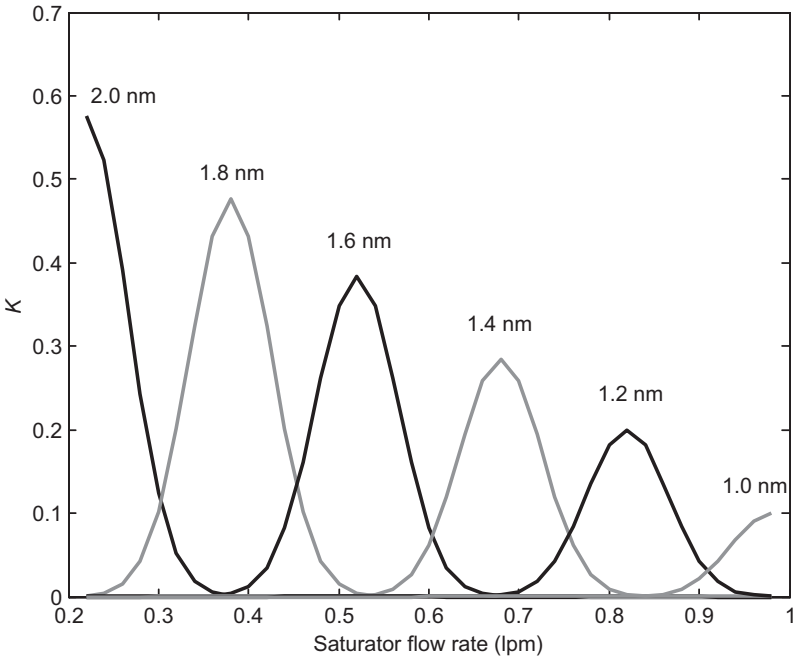

Fig. 5. Gaussian-shaped kernel functions used for the data inversion. The height and width of the kernels for each size where chosen so as to resemble the measurement data in Fig. 4. (derivative of cut-off curves 0.2 nm apart).

Data treatment and inversion

Based on the calibrations, described in the previous section, a data inversion was developed in order to convert the data measured with the PSM in scanning mode into a size distribution. Two different methods for data inversion were tested: step-wise method and Gaussian method. Before the data inversion, we removed peaks in the concentration data, and smoothed the data e.g. with a moving average filter, for minimizing the effect of fluctuations, which are faster than the 120 s scan cycle. Each scan was then treated separately.

In the step-wise method, we assumed a step-function like activation curve for each size, i.e. all particles of a certain size activate exactly at a certain saturator flow rate. The total concentration was then taken at seven different saturator flow rates between 0.2 and 1 lpm, which correspond to cut-off sizes 0.9–2.1 nm (*see* Fig. 4b). The concentration in each size bin limited by these cut-off sizes was calculated as the difference in the concentration on the upper and lower limit of the size bin. The difference was then corrected for the average detection efficiency at the mean diameter of that size bin as follows:

$$C\left(d_{\mathrm{p}}\right)=\frac{C_{\mathrm{upper}}-C_{\mathrm{lower}}}{D\left(d_{\mathrm{p}}\right)}, \qquad (1)$$

where $C(d_{\mathrm{p}})$ is the concentration in the size bin, C_{upper} is the concentration at the upper limit of the size bin, C_{lower} is the concentration at the lower limit of the size bin, $D(d_{\mathrm{p}})$ is the detection efficiency and d_{p} is the particle diameter.

In the Gaussian inversion method, we used Gaussian-shaped kernel functions (*see* Fig. 5) for inverting the data. The kernel functions describe the probability of particles of a certain size being measured at a certain flow rate. Thus the measured concentration in a size bin is the sum of the actual concentrations multiplied by the kernel functions. The width and height of the kernel functions were chosen so that they resemble the difference between the measured activation curves (Fig. 4a), taking the detection efficiency into account. We chose to use six channels 0.2 nm apart from each other, so that the kernel functions do not overlap too much. Now the concentration in each size bin can be calculated using matrix inversion for the measured concentration at each saturator flow bin as follows [for the inversion we used a least-squares inversion routine (MATLAB function *lsqnonneg*)]:

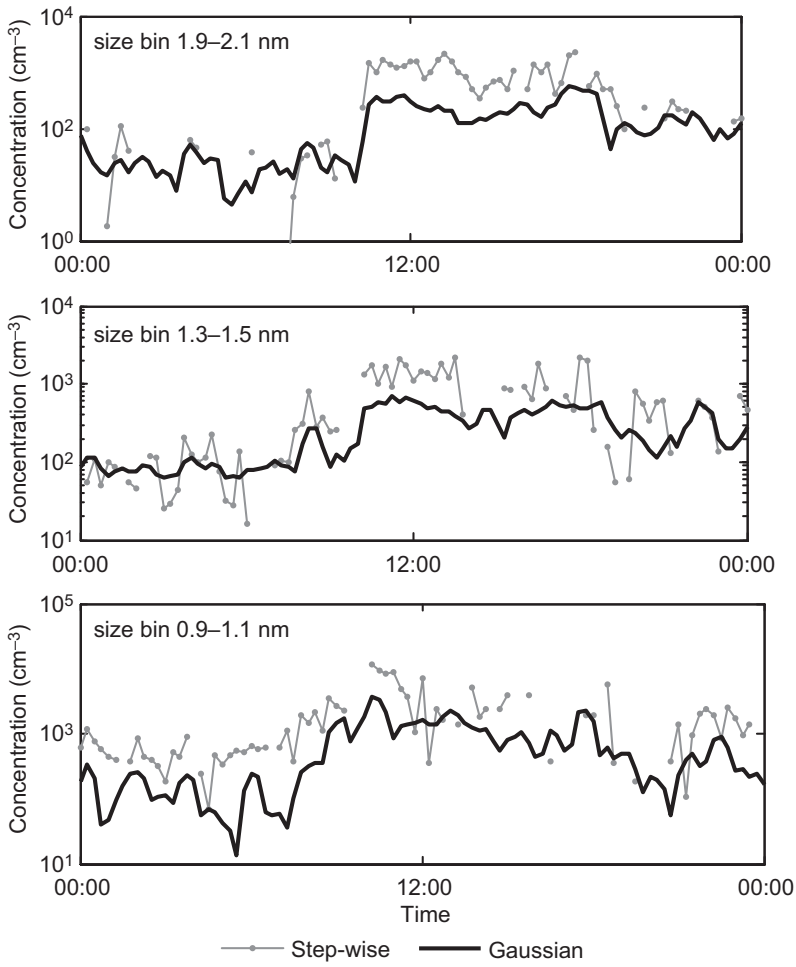

Fig. 6. Testing different inversion methods for the PSM data. The data were divided into size bins assuming either step-wise cut-off functions (gray dots) or Gaussian-shaped kernel functions (black line). The test data set is a one-day measurement (31 Mar. 2011) with the PSM at the Hyytiälä SMEAR II station.

$$C_{\mathrm{meas}}\left(f_{\mathrm{sat}}\right) = \int_0^\infty P\left(d_{\mathrm{p}}\right) C_{\mathrm{true}}\left(d_{\mathrm{p}}\right) dd_{\mathrm{p}} = \sum K\left(f_{\mathrm{sat}}\right) C_{\mathrm{true}}\left(d_{\mathrm{p}}\right), \quad (2)$$

where C_{meas} is the measured concentration at a certain saturator flow rate (f_{sat}), P is the probability of a certain sized particle (d_{p}) to be measured at that saturator flow rate, C_{true} is the true concentration of particles of certain size, and K is the kernel function. Measurement errors were not considered in the inversion, which should be kept in mind especially when the noise-to-signal ratio is high.

The two inversion methods are compared in Fig. 6 for one day of field measurement data. The output of the step-wise inversion method seemed to be more noisy than that of the Gaussian method, giving somewhat higher concentrations during the nucleation event (indicated by the high concentration of small particles between about 10 am and 3 pm) and in the smallest channel, but also negative values when the concentration was low. The least-squares inversion function forces the result to be non-negative, which is a justified assumption for particle concentration data. However, both methods showed similar time trends in the data and captured the starting of the nucleation event. We compared the size distributions obtained using the least-squares inversion method with the size distribution measured with the NAIS. An example with the size distributions merged is shown in Fig. 7a (the size range 0.9–2.1 nm was measured with the PSM and 3–40 nm with NAIS).

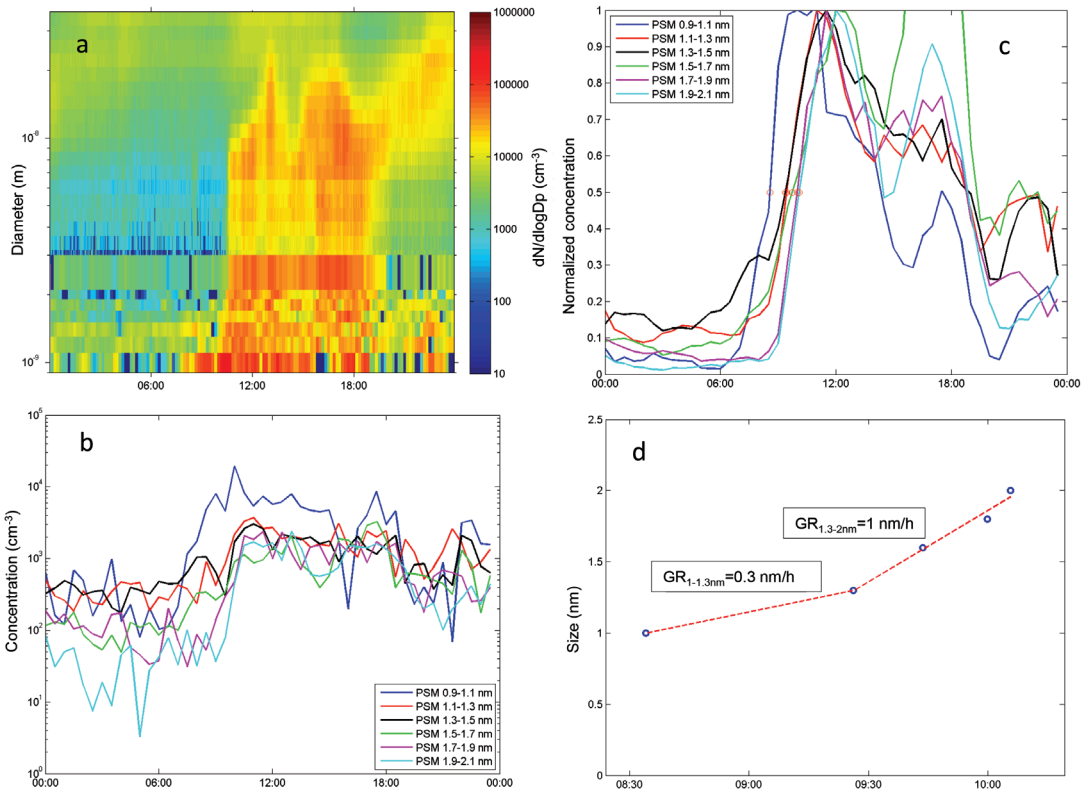

Fig. 7. A nucleation event day (31 Mar. 2011) at SMEAR II in Hyytiälä. (**a**) A composite size distribution from the PSM (0.9–2.1 nm) and NAIS (3–40 nm). The concentration between 2.1 and 3 nm was obtained from the difference between the total concentration measured with the PSM at 2.1 nm cut-off size (2.1–1000 nm) and the total concentration from the DMPS (3–1000 nm). (**b**) The concentration in each size bin of the PSM determined with the Gaussian inversion method. (**c**) Normalized concentration in each size bin (maximum concentration in each bin set to 1); the 50% appearance times of the particles are marked with red cirles. (**d**) The GRs determined with the appearance time method $GR_{sr,50}$ for two separate size classes 1–1.3 nm and 1.3–2 nm.

Determining the growth rates

Appearance time method

After the start of a nucleation event, both in the atmosphere and in the laboratory, the recently-formed particles normally grow in size by condensation of the nucleating vapours and possibly also other vapours. Thus the particle size distribution evolves as the particles move into larger size bins as they grow. The apparent growth rate (GR, normally expressed in nm h^{-1}) can be determined by following this time evolution. Here, we define "the appearance time method" for determining initial particle growth rates. The method is based on finding the time step when the newly-formed particles appear at a certain size, and calculating the GR from the time difference between successive sizes.

It is not obvious how the time steps should be chosen for the appearance time method. We tested four different options for selecting the time step for each size: (1) the time when the (total) concentration at certain cut-off size increased to 5% from the maximum concentration reached during nucleation, hereafter called $GR_{tot,5}$; (2) the time when (total) concentration reached 50% of the maximum, hereafter called $GR_{tot,50}$; (3) the time when the concentration in a certain size bin has increased to 5% of the maximum, hereafter called $GR_{sr,5}$; (4) the time when the concentration in a certain size bin has reached 50% of the maximum, hereafter called $GR_{sr,50}$. To follow the leading edge of the distribution ($GR_{tot,5}$ and $GR_{sr,5}$),

any (low) percentage value could be used, we for consistency chose 5%. The appearance time method is not restricted to PSM data, but can be used with any data set where particle measurements at several size limits or several size bins exist, e.g. a CPC battery with several CPCs measuring at different cut-off sizes. This is sometimes called a time-lag method (e.g. Riccobono *et al*. 2012). However, if the shapes of the cut-off curves of the instruments are very different, the time-lag method might considerably under- or overestimate the GR (Riccobono *et al*. 2012).

We determined the GR using $GR_{sr,50}$ which was applied to the field measurement data (*see* Fig. 7b and c). From there, we can find the time steps at which the concentration reached 50% of its maximum value in each size bin (represented with the mean diameter of the size bin). The GR was then determined as a linear fit between the 50% time steps and the mean diameters. For studying the size dependency of the growth rate, the fitting can be done separately for different size ranges, as in Kulmala *et al*. (2013). In the example case (*see* Fig. 7d), $GR_{sr,50}$ = 0.3 nm h^{-1} for the particles size range 1–1.3 nm, and $GR_{sr,50}$ = 1.0 nm h^{-1} for 1.3–2 nm.

For the data measured in the chamber experiments in CLOUD, we determined the growth rate by following the leading edge of the size distribution ($GR_{tot,5}$). This method describes the growth of the most rapidly growing particles, and it was suitable for CLOUD experiments, in which the chamber was in most cases almost clean of particles before the start of the experiment, and the particle formation reached a steady-state situation quickly (Kirkby *et al*. 2011). This method is visualized in Fig. 8. The total particle concentrations at the different saturator flow rates after the start of a nucleation experiment are shown Fig. 8a. The concentration was slightly decreasing before the start of nucleation due to removal of larger particles in the chamber. Here, we also first normalized the data and searched for the time step when the concentration had increased to 5% of the maximum. The GR was determined by a linear fit between the time steps and the cut-off diameters. The advantage of this method is that the data do not need to be inverted into a size distribution before determining the GR, so it is applicable also when just total concentration data at 2 or more cut-off sizes exists.

The $GR_{sr,50}$ and $GR_{tot,5}$ are compared in Fig. 8b. The 50% values are naturally reached later, but the resulting GRs are close to each other: 2.6 nm h^{-1} from $GR_{tot,5}$ and 2.1 nm h^{-1} from $GR_{sr,50}$. For comparison, also the 50% appearance times of ion clusters identified and measured with the APi-TOF mass spectrometer (Junninen *et al*. 2010, Schobesberger *et al*. 2013) are shown, and the 50% times for each size bin from the NAIS data. NAIS and the APi-TOF gave GRs of 2.0 nm h^{-1} and 2.3 nm h^{-1}, respectively. The correlation between the GRs measured with the PSM ($GR_{tot,5}$) and NAIS (50% appearance time) was generally good (r = 0.88, *see* Fig. 9). It should be noted that NAIS was used in ion mode so it detected only ions, whereas the PSM measured both ions and neutral particles. Of the different versions of the appearance time method, $GR_{sr,50}$ is closest to the mode-fitting method or maximum concentration method used traditionally with the size spectrometer data sets (Yli-Juuti *et al*. 2011). However, the appearance time method has been found to work also when the size distribution has not yet formed a clear mode, or the concentrations are very low, which often inhibits the use of the traditional methods at very small sizes and especially in the beginning of the nucleation process.

The appearance time method simulation study

The appearance time method, described above, was tested by using the method on the data obtained from a set of aerosol dynamics simulations. The principal idea is that we know the growth rate of particles in the simulation and we can estimate the growth rate from the output data of the simulations, so comparing the "real" value obtained directly from the simulation and the "estimate" obtained using the appearance time method, we can assess how well the method is able to estimate the growth rate. More specifically, the aims of the simulation study were to assess (1) how the uncertainty in the shape of the detection efficiency curves, e.g. due to changes in particle composition, is affecting the determination of the GRs, (2) how well the method is

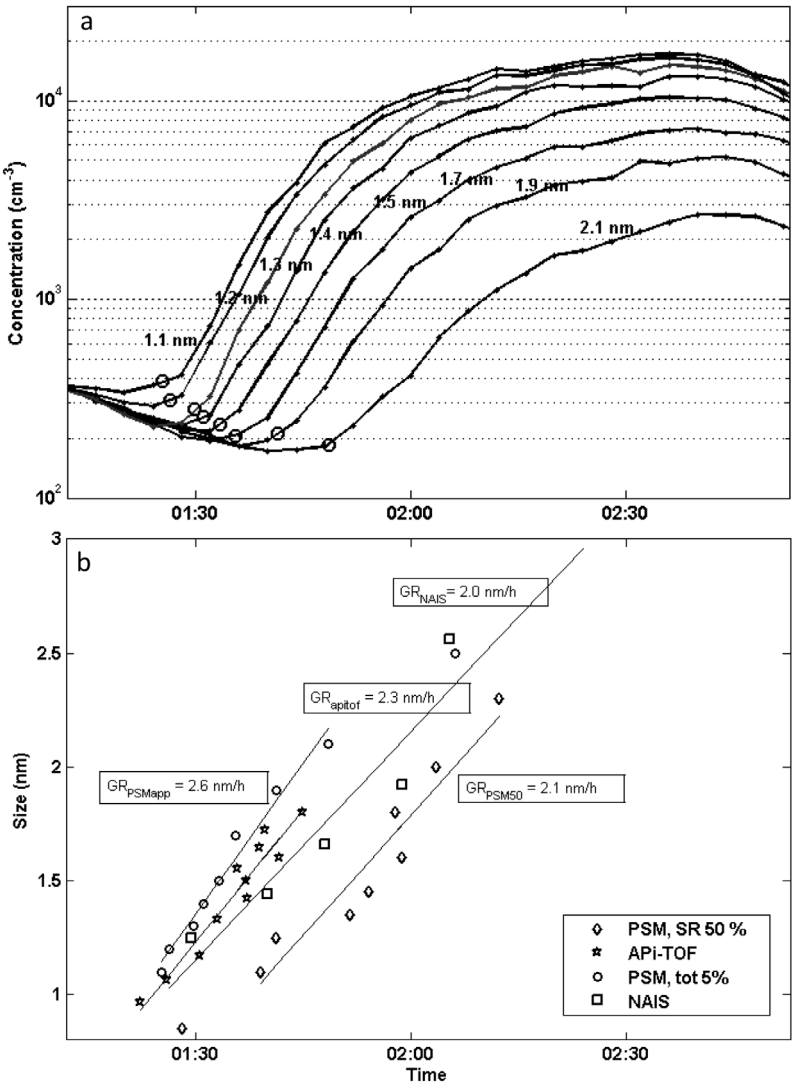

Fig. 8. Example of a nucleation experiment in the CLOUD chamber. (**a**) Concentrations measured at different cut-off sizes of the PSM. After starting of the experiment, each channel starts detecting particles after a different time lag depending on the cut-off size, and the time steps when the concentrations have increased to 5% of maximum are indicated with a circle. Panel **b** shows the GRs calculated from the PSM both with $GR_{tot,5}$ and $GR_{sr,50}$, and the GRs from the NAIS (negative ion mode) and APi-TOF data (negative ions) for comparison. Symbols are in the middle points of each size bin, and lines are linear fits to the measurement points.

able to capture the size dependency of the GR, and (3) in what conditions the GR can be reliably determined using the appearance time method.

Methodology of the simulation study

The simulations were conducted using the Ion-UHMA (University of Helsinki Multicomponent Aerosol Model for neutral and charged particles) model (Leppä *et al*. 2009). The simulated particle diameter range was from 1.0 to 50.0 nm and the range was covered by 120 size sections distributed evenly on a logarithmic scale. Furthermore, depending on their electric charge the particles were divided into three classes: neutral, negatively-charged and positively-charged. Besides the particles, the simulations included pools for negatively- and positively-charged small ions. The mobility of the negative (positive) small ions was assumed to be 1.6 (1.4) $cm^2\ V^{-1}\ s^{-1}$ which corresponds roughly to a mobility diameter of 1.14 (1.22) nm (Ehn *et al*. 2011). For both polarities, the concentrations of small ions were kept constant at 400 cm^{-3}. The particle number size distribution for each charge class was obtained as an output from the simulations with a time resolution of 30 s.

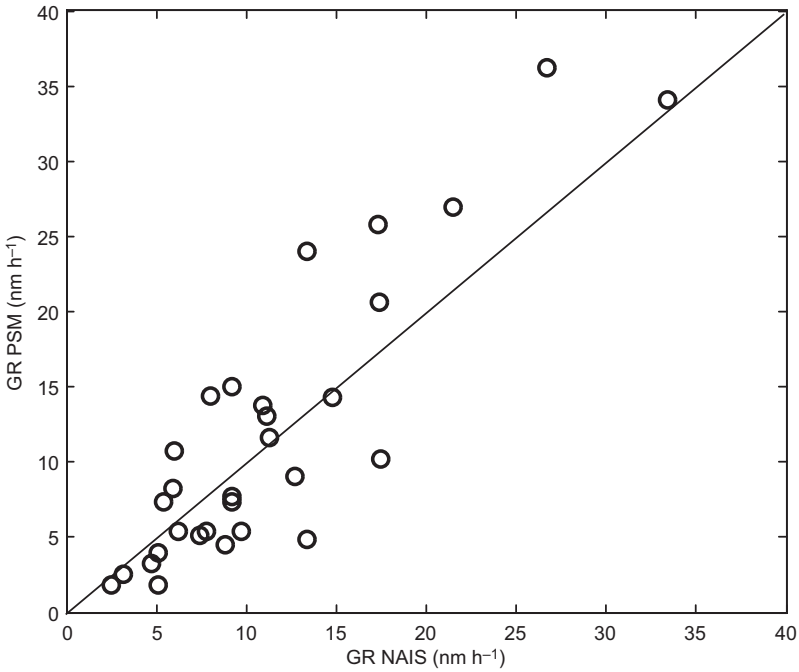

Fig. 9. A data set of 30 nucleation experiments from CLOUD during October–November 2010, where GR could be calculated both from the PSM ($GR_{tot,5}$) and NAIS (1.5–3 nm negative ions). The correlation coefficient (r) between these two data sets was 0.88. The 1:1 line is plotted to guide the eye.

The main processes modelled in the simulations were the new particle formation (NPF), condensational growth of the particles, coagulation and ion-aerosol attachment. The actual nucleation process was, however, not simulated, but the formation rate of particles with 1 nm in diameter, J_1, was used as input in the simulation. The value of J_1 was either kept constant or followed a sinusoidal pattern as a function of time with the average rate of either 1 cm^{-3} s^{-1}, which correspond roughly to a typical value observed at Hyytiälä (Manninen *et al*. 2009), or 100 cm^{-3} s^{-1} which could be observed in a more polluted urban environment (Kulmala *et al*. 2004), respectively. The duration of the NPF was either 1 or 4 hours, which correspond to short, burst-like, NPF events or to NPF events spanning over a considerable time period, respectively.

The majority of the particles were formed electrically neutral with the fractions of particles formed negatively- or positively-charged being 5% per polarity. In total, 10% of the particles were assumed to be formed via ion-induced nucleation, IIN, which corresponds roughly to an average value of the IIN observed at Hyytiälä (Manninen *et al*. 2010).

Rather than simulating the condensation process, the particle diameter growth rate was used as input in the simulations with optionally different growth rates for neutral (GR_0) and charged ($GR_\pm$) particles. In all simulations, the growth rates were kept constant in time. As a function of diameter, the GR_0 had either a constant value of 5 nm h^{-1} or increased according to

$$GR_0\left(d_p\right) = 5 \times \tanh\left[0.17\left(d_p + 0.8\right)\right], \quad (3)$$

where d_p is the diameter in nanometres and GR_0 is obtained in nm h^{-1}. The functional form of the diameter dependence of the GR_0 was arbitrarily chosen, but it is similar to that observed in field measurements (Hirsikko *et al*. 2005, Yli-Juuti *et al*. 2011, Kuang *et al*. 2012b). $GR_\pm$ was either the same as GR_0 or was multiplied by a charge enhancement factor, $\xi(d_p)$, which was calculated according to Nadykto and Yu (2003) and by assuming that the condensing molecule had properties similar to the sulphuric acid molecule. These growth rates and the enhancement factor as a function of diameter are plotted in Fig. 10.

Finally, there were four different options for a particle sink in the simulations: (1) no sink; (2) particles removed by the loss rate $S(d_p)$ =

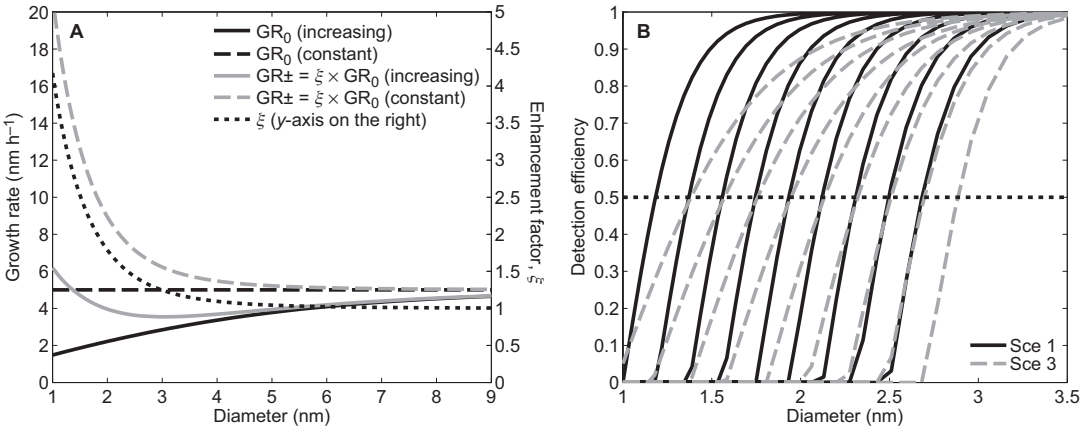

Fig. 10. (**A**) The growth rates of neutral (black) and charged (grey) particles used as inputs in the model; the enhancement factor, ξ, values are also shown. (**B**) The detection efficiency curves in Scenarios 1 and 3 used to obtain measurement-like data from simulated data. The crossing of detection efficiency curve and the dotted line marking detection efficiency of 0.5 denote the diameter attributed to that detection efficiency curve.

(1.31×10^{-3} nm/d_p) s^{-1}; (3) coagulation loss to pre-existing larger particles modelled by adding a monodisperse distribution with the concentration of 320 cm^{-3} and particle diameter of 150 nm; (4) the same as option 3, but with the concentration of 3200 cm^{-3}. Option 2 provides a loss rate similar to the estimated wall losses occurring in the CLOUD chamber in CERN (Almeida *et al*. 2013). Options 3 and 4 provide the condensation sinks (CS) values of 1×10^{-3} s^{-1} and 1×10^{-2} s^{-1}, which are a typical and a rather high value, respectively, when compared with those observed at Hyytiälä (Dal Maso *et al*. 2007).

All combinations of the options listed above were included in the simulations resulting in 128 simulations (for the values of input parameters used in the simulations *see* Table 1). It should be noted that this simulation set does not provide a representative sample of the covered parameter space, i.e. it can be used to characterize features of the appearance time method, but it is not suitable for detailed statistical analysis.

Before applying the appearance time method, the simulated data was converted to a format emulating the data format obtained from the PSM. This was achieved by assuming a set of detection efficiency curves with each curve corresponding to a different cut-off size (Fig. 10B). Four sets of nine curves were used providing the following scenarios:

Scenario 1: The shape of a detection efficiency curve was similar to that assumed for the PSM and the same for each curve. The cut-off sizes ranged from 1.18 to 2.68 nm and were equally spaced in the diameter space.

Scenario 2: The same as Scenario 1, but the curves were linearly-shifted towards larger sizes by 0.5 nm (range from 1.68 nm to 3.18 nm).

Scenario 3: The shape of the curves changed as a function of cut-off size with the slope of the curve steepening with increasing cut-off size. The cut-off sizes were 0.2 nm greater than in Scenario 1, i.e. ranging from 1.38 to 2.88 nm.

Scenario 4: The curves were assumed to be step-functions with the steps occurring at the same cut-off sizes as in Scenario 1.

Scenarios 1 and 4 correspond to detection efficiency curves obtained using the Gaussian and step-wise inversion methods (*see* section 'Data treatment and inversion'), respectively. Scenario 2 characterizes a situation in which the particles activated in the PSM are actually larger than expected, for example due to a difference in the composition of the measured particles and those used to calibrate the instrument. Scenario 3 characterizes a situation in which the shapes of the detection efficiency curves depend on the cut-off size, which could also be due to differences in the particle composition.

Applying these detection efficiency curves to the simulated particle number size distribution provided a time evolution of total particle concentration corresponding to each cut-off size. The size-resolved concentrations were then calculated as a difference between the total concentrations corresponding to two consecutive cut-off sizes. This provided time evolution of the concentrations in eight size ranges and the arithmetic mean of each size range was assigned as the diameter corresponding to that range. The growth rates were then determined using each of the four versions of the appearance time method ($GR_{tot,5}$, $GR_{tot,50}$, $GR_{sr,5}$ and $GR_{sr,50}$; *see* section 'Apearance time method'). These four growth rates were determined from all combinations of simulation and detection efficiency curve scenarios. Furthermore, the four GRs were determined for the lower (1.18–1.93 nm) and upper (1.93–2.68 nm) halves of the size range for each simulation using the detection efficiency curves of Scenario 1. All in all, this resulted in 24 growth rates being determined for each simulation (4 Scenarios × 4 methods + 2 size ranges × 4 methods), and these are collectively denoted as 'the determined growth rates'.

For each determined growth rate, we calculated a corresponding growth rate in the simulation, namely simulated growth rate. Simulated growth rates were not the same as the values of the growth rate used as input in the simulation. The growth rate in most of the simulations varied both as a function of particle diameter and/or as a function of time for either or both of the following reasons: (1) the GR_0 used as input varied as a function of diameter, and (2) the charged particles grew by a different rate than the neutral ones. In order to calculate a single value of simulated growth rate, we first calculated an average growth rate, GR_{ave}, as follows:

$$GR_{ave}\left(d_p,t\right)=\frac{3}{1+\lambda+\lambda^2}\times\left\{\begin{array}{l}\chi_{\pm}\left(d_p,t\right)\times GR_{\pm}\left(d_p\right)\\+\left[1-\chi_{\pm}\left(d_p,t\right)\right]\times GR_0\left(d_p\right)\end{array}\right\}, \quad (4)$$

where t is the time, λ is the ratio of two consecutive diameters in the diameter grid of the Ion-UHMA model (in this study, $\lambda \approx 0.967$) and $\chi_{\pm}$ is the total fraction of charged particles. The first term on the right-hand side of Eq. 4 takes into account the numerical diffusion occurring in Ion-UHMA (Leppä *et al*. 2011). According to Eq. 4, GR_{ave} provides an estimate of the average condensational growth rate, but does not take into account growth due to coagulation processes occurring in Ion-UHMA.

The simulated growth rate corresponding to a determined growth rate was calculated as the time it would take for a particle to grow from the smallest diameter to the largest diameter in the diameter range that was used for the determined growth rate. For example, if the determined growth rate was obtained using data points, (t,d_p), in the diameter range from 1.18 to 2.68 nm and the first data point was (1.2 h, 1.18 nm), then the corresponding simulated growth rate, GR_{sim}, would be

$$GR_{sim}=\frac{d_{p,2}-d_{p,1}}{t_2-t_1}=\frac{2.68\,\text{nm}-1.18\,\text{nm}}{t_2-1.2\,\text{h}}, \quad (5)$$

where t_2 is the moment of time at which a par-

Table 1. The values of the parameters used as inputs in the Ion-UHMA simulations. Here J_1 is the average NPF rate, GR_0 and $GR_{\pm}$ are the growth rates of neutral and charged particles, respectively, and ξ is the enhancement factor (Fig. 10A). Options for particle losses in the simulations were (1) no losses, (2) wall losses similar to those occurring in the CLOUD experiment, and (3 and 4) coagulation scavenging by particles with a diameter of 150 nm and with concentrations corresponding to values of CS provided in the table.

Parameter	Option 1	Option 2	Option 3	Option 4
J_1 (cm^{-3} s^{-1})	1	100	–	–
Duration of NPF (h)	1	4	–	–
J_1 as a function of time	Constant	Sinusoidal	–	–
$GR_0(d_p)$ (nm h^{-1})	5	$5\times\tanh[0.17\times(d_p+0.8)]$	–	–
$GR_{\pm}(d_p)$ (nm h^{-1})	$GR_0(d_p)$	$\xi(d_p)\times GR_0(d_p)$	–	–
Particle losses (s^{-1})	0	1.31×10^{-3} nm/d_p	CS = 1×10^{-3}	CS = 1×10^{-2}

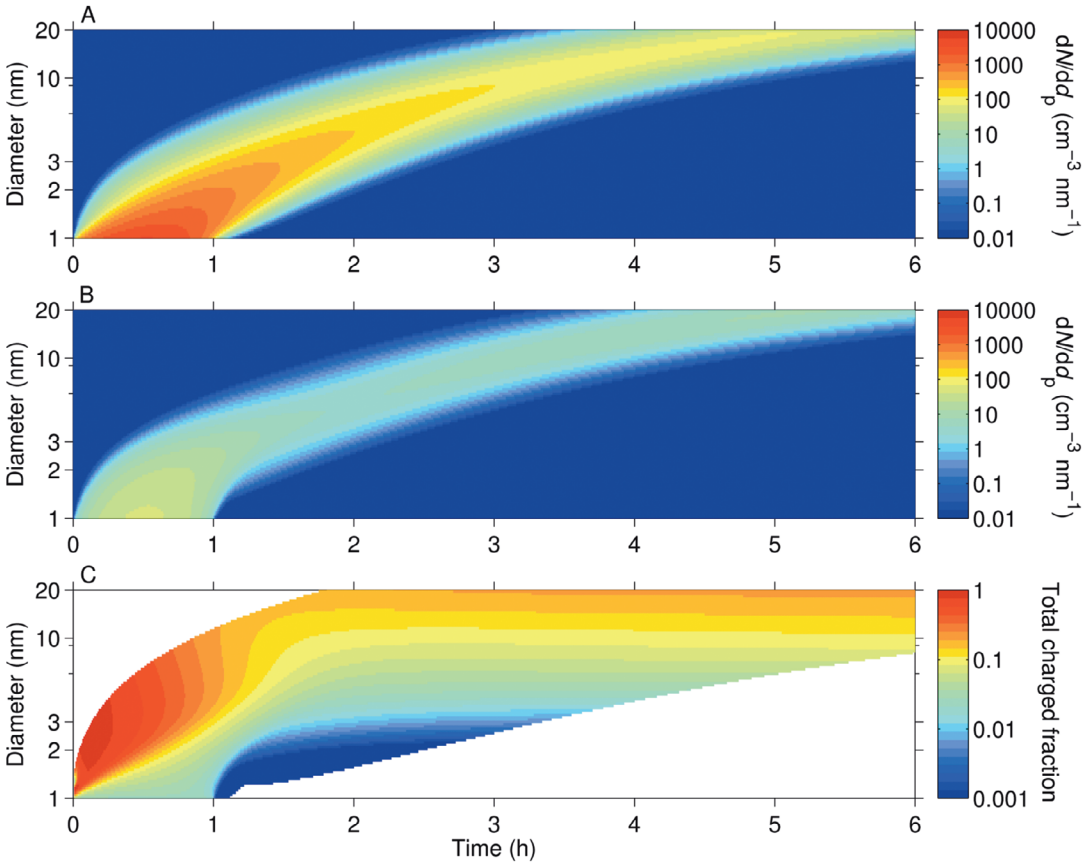

Fig. 11. Time evolution of particle number size distribution for (**A**) total and (**B**) negatively-charged particles in the example simulation. (**C**) Total fraction of charged particles as a function of time and diameter in the example simulation.

ticle starting at (1.2 h, 1.18 nm) and growing by rate $GR_{ave}(t,d_p)$ would reach the diameter of 2.68 nm.

Determined and simulated growth rates in an example simulation

An example of the time evolution of a particle number size distribution obtained as an output from a simulation is shown in Fig. 11. In this simulation, GR_0 increased as a function of diameter, $GR_{\pm}$ was $\xi \times GR_0$, the NPF rate followed a sinusoidal pattern with duration of 1 h and average rate of 1 cm^{-3} s^{-1}. The proportion of the IIN in the simulation was 10%, 5% per polarity. However, because the charged particles grew more rapidly than the neutral ones, a very high fraction of charged particles was observed in the beginning of the simulation and the charged fraction at the size of the particle formation, 1 nm, was much smaller than 0.1 (Fig. 11). These phenomena have been explained in detail by Leppä *et al*. (2013).

The size-resolved concentrations and total concentrations corresponding to different cut-off sizes obtained using the detection efficiency curves of Scenario 1 on the output data of the example simulation are plotted in Fig. 12. It should be noted that the size-resolved concentrations reached 5% and 50% of their maximum values earlier than did the total concentrations with the corresponding cut-off sizes (*see* Fig 13A).

In the example simulation, the GR_{ave} value varied considerably as a function of time and diameter (Fig. 13). It was especially high at the beginning of the simulation, which results from

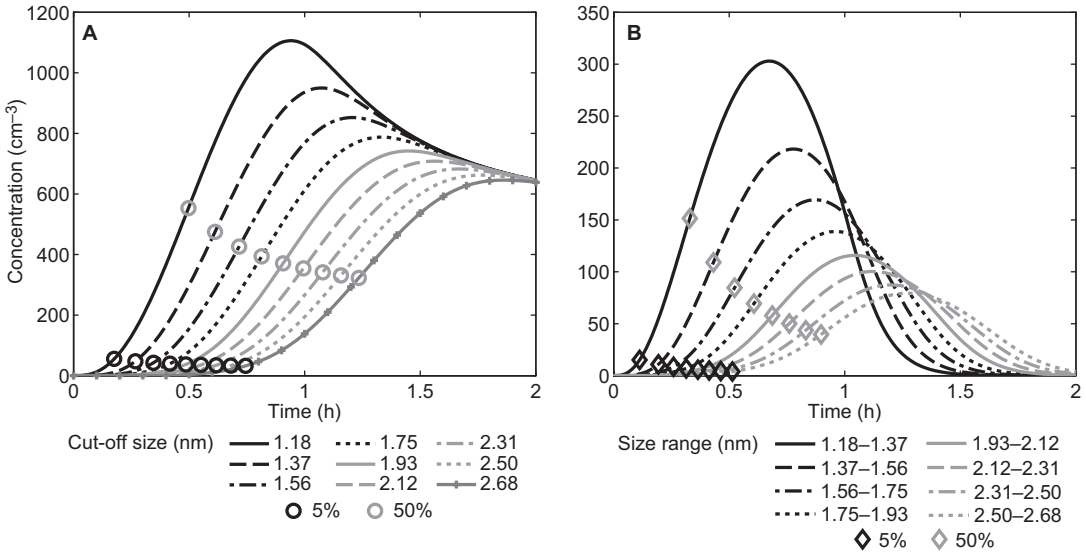

Fig. 12. (**A**) The total particle number concentration in the example simulation as observed using detection efficiency curves in Scenario 1; 5% and 50% of the maximum values are indicated with circles. (**B**) The size-resolved concentrations of different size ranges; 5% and 50% of the maximum values are indicated with diamonds.

high proportion of charged particles (Fig. 11) and charged particles growing more rapidly than the neutral ones.

In the example case, all the four versions of the appearance time method provided a growth rate close to the corresponding simulated growth rate (Fig. 13B). Furthermore, $GR_{sr,5} > GR_{tot,5} > GR_{sr,50} > GR_{tot,50}$ because the time values of the data points used to determine $GR_{sr,5}$, $GR_{tot,5}$, $GR_{sr,50}$ and $GR_{tot,50}$ were in that same order from the beginning of the simulation and the value of GR_{ave} was the highest towards the beginning of the simulation (Fig. 13). However, it should be noted that none of the four versions of the appearance time method was able to produce a value as high as $GR_{\pm}$.

Effect of changes in the detection efficiency curves on the determined growth rates

The determined growth rates obtained using detection efficiency curve Scenarios 2, 3 and 4 were within a factor of 1.2 from the corresponding growth rate determined using Scenario 1 for a vast majority of simulations regardless of which version of appearance time method was used (Fig. 14). On average, the values of $GR_{tot,5}$, $GR_{sr,50}$ and $GR_{tot,50}$ determined using Scenario 2 were slightly higher than those determined using Scenario 1 (Table 2). This resulted from the simulations with GR_0 increasing as a function of diameter: since cut-sizes corresponding to Scenario 2 were greater than those corresponding to Scenario 1 and the growth rate was higher at the larger sizes, the GRs determined using Scenario 2 were higher than those using Scenario 1. This phenomenon held true also for $GR_{sr,5}$, but the $GR_{sr,5}$ values were affected by an opposite phenomenon also: when the charged particles grew more rapidly than the neutral ones, the values of GR_{ave} decreased as a function of diameter, especially at the beginning of the simulation (Fig. 13). This latter phenomenon was more pronounced for $GR_{sr,5}$ than for $GR_{tot,5}$, $GR_{sr,50}$ and $GR_{tot,50}$, because $GR_{sr,5}$ was determined using data closest to the beginning of the simulation. With these two phenomena being approximately equal in the case of $GR_{sr,5}$, at least for the simulation set used in this study, the values of $GR_{sr,5}$ determined using Scenarios 1 and 2 were approximately the same.

On average, the values of GR determined using Scenario 3 were smaller than those determined using Scenario 1, especially in the case of $GR_{sr,5}$ (Table 2). The phenomenon causing

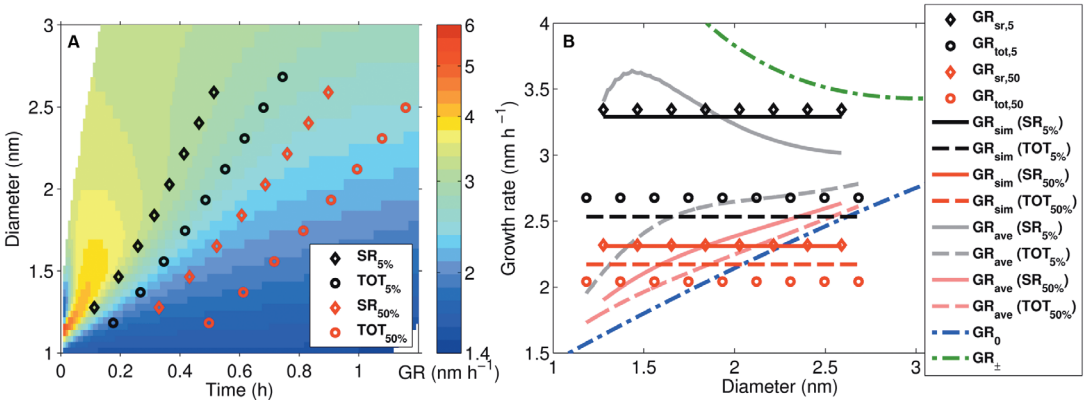

Fig. 13. (**A**) The value of $GR_{ave}(d_p,t)$; the time when the size-resolved concentrations (SR) and total concentrations (TOT) reached 5% and 50% of their maximum values in the case of Scenario 1 being used for the detection efficiency curves are also shown. Note that diamonds and circles in **A** correspond to diamonds and circles in Fig. 12, except that the time values are plotted against the cut-off diameters instead of concentration. (**B**) Growth rates in the example simulation; the values of $GR_{ave}(d_p,t)$ with d_p and t corresponding to the data points marked in **A** are also shown.

this discrepancy was described in detail by Riccobono *et al*. (2012). In this study, the ratio of GRs determined using Scenarios 3 and 1 varied between 0.81 and 1.09. This provides a rough estimate on how much the assumed difference in the shape of detection efficiency curves could affect the determined growth rate.

Finally, the values of GR determined using Scenario 4 were, on average, slightly higher than those determined using Scenario 1, especially in the case of $GR_{sr,5}$ (Table 2). The ratio of GRs determined using Scenarios 4 and 1 varied between 0.98 and 1.12. In other words, using detection efficiency curves corresponding to Gaussian or step-wise inversion methods had rather little effect on the growth rate determined with the appearance time method.

Determining the size dependency of the growth rate

The distributions of the GR ratios determined for the upper (1.93–2.68 nm) and lower (1.18–1.93 nm) halves of the diameter range, when using detection efficiency curves corresponding to Scenario 1 are plotted in Fig. 15 for each version of the appearance time method. For each method, the determined growth rates and the corresponding simulated growth rates had a similar distribution indicating that the methods were able to capture the actual diameter dependence occurring in the simulation. Furthermore, the peaks of the distributions for simulations with and without the diameter dependence in the growth rate of neutral particles occurred at 1.3 and 1.0, respectively, which match the diameter dependence, or lack of one, used as input in the simulation. The values smaller than the peaks in the corresponding distributions (*see* Fig. 15) correspond to the simulations in which the charged particles grew more rapidly than the neutral ones, which caused the growth rate in the simulation to decrease as a function of diameter (*see* Fig. 13). This was most pronounced in the case of $GR_{sr,5}$ since the data points used to determine those values were closest to the beginning of the simulation and the effect of enhanced growth of charged particles was most pronounced towards the beginning of the simulation.

Comparison of simulated and determined growth rates in different conditions

In the cases of highest coagulation sink used in the simulation, the methods tended to provide values that did not match the corresponding simulated ones (*see* Fig. 16). Whether the method underestimated or overestimated, as well as how systematic the error was, depended on

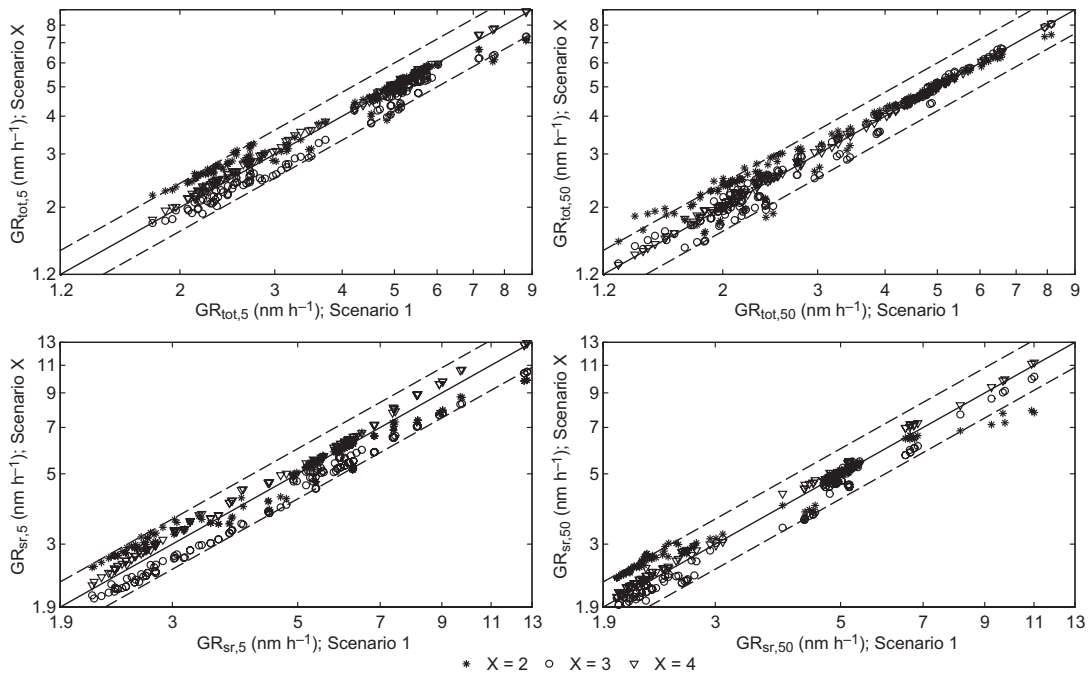

Fig. 14. Growth rates determined assuming detection efficiency curves in Scenarios 2, 3 and 4 (different symbols) as a function of corresponding growth rates determined in Scenario 1. Solid and dashed lines denote 1:1 correspondence and a difference by a factor of 1.2, respectively. The panels show results for different versions of appearance time method (*see* the axis labels).

the method. In this regard, the $GR_{sr,50}$ was the most robust method with all the values being within a factor of 1.6 of the corresponding simulated value.

When GR_0 increased as a function of diameter in the simulation, all the methods provided higher GR in the case of J_1 being 100 cm^{-3} s^{-1} instead of 1 cm^{-3} s^{-1}. For the values of $GR_{tot,5}$ and $GR_{tot,50}$, this was also observed when GR_0 was constant. This indicates that the determined values were affected by self-coagulation occurring in those simulations. The magnitude of this increase in GR caused by self-coagulation was in line with the results by Leppä *et al*. (2011).

Overall, the most robust methods to determine the simulated growth rate were the $GR_{tot,5}$ and $GR_{sr,50}$. When comparing these two methods, the latter was more robust if the coagulation sink was high, but considerably overestimated GR, if the NPF rate followed a sinusoidal pattern for

Table 2. The average of ratios of growth rates determined assuming detection efficiency curves of Scenarios 2, 3 and 4 (indicated by X) to the corresponding growth rates determined assuming detection efficiency curves of Scenario 1. In the first column on the left it is indicated whether the average is calculated over all simulations or over a subset of simulations with the given characteristic.

Simulations	Scenario X/Scenario 1	$GR_{sr,5}$	$GR_{tot,5}$	$GR_{sr,50}$	$GR_{tot,50}$
All	X = 2	1.01	1.04	1.05	1.06
All	X = 3	0.89	0.93	0.94	0.98
All	X = 4	1.05	1.02	1.03	1.01
GR_0 constant	X = 2	0.97	1.00	0.98	1.01
GR_0 increasing	X = 2	1.06	1.09	1.12	1.12
$GR_\pm = GR_0$	X = 2	1.06	1.08	1.06	1.08
$GR_\pm = \xi \times GR_0$	X = 2	0.97	1.01	1.03	1.05

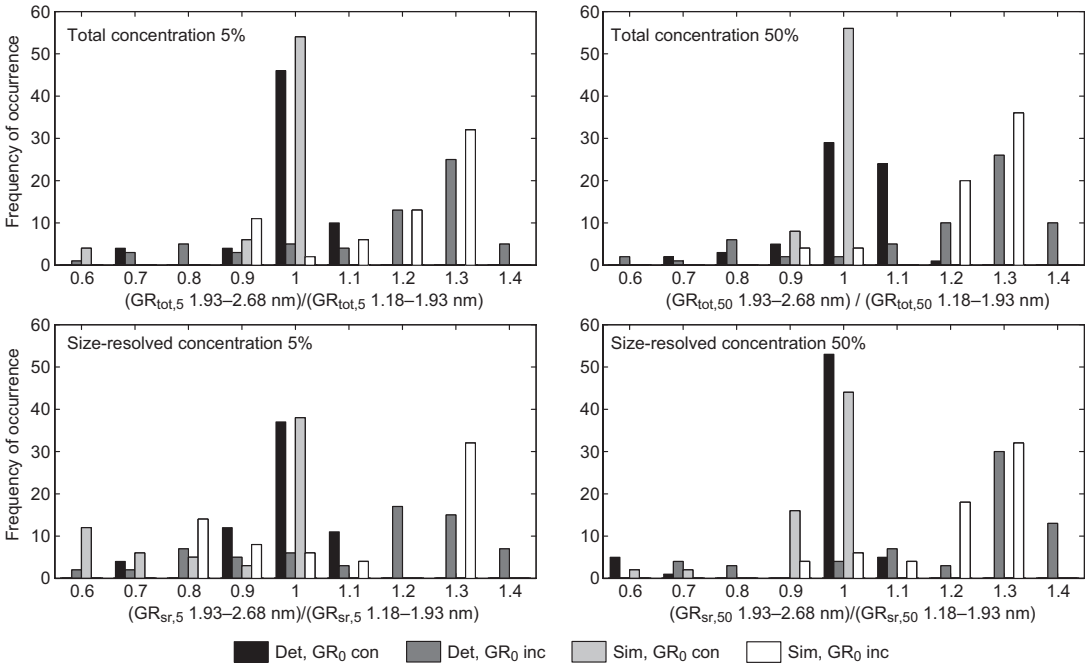

Fig. 15. Distributions of ratios of growth rates determined for the upper and lower halves of the diameter range, from 1.93 to 2.68 nm and from 1.18 to 1.93 nm, respectively. The GRs were determined using the appearance time method (Det) or they are corresponding simulated values (Sim) and the value of GR_0 used as input in the simulation was constant (con) or increased as a function of diameter (inc). Different panels correspond to different versions of the appearance time method.

4 h with the average J_1 being 100 cm^{-3} s^{-1}, especially if GR_0 was constant.

Conclusions

We have developed methods to obtain the particle size distribution and growth rates in the size range below 3 nm using the data measured with the Particle Size Magnifier in scanning mode. We have shown that the activation curves of ammonium sulphate particles with 0.1 nm difference in diameter are clearly separable in the size range of 1–2 nm, and therefore a data inversion can be developed. We tested and compared two inversion methods for obtaining the size distribution, of which the method based on Gaussian-shaped kernel functions seem to work best for real measurement data. We then introduced the appearance time method for calculating the growth rate of particles, and tested which is the best way of selecting the appearance times from measurement data.

Converting the measurement data into a size distribution or growth rate requires careful calibration of the instrument, and some assumptions about the particle composition. Changes in the composition of the particles, and changes in conditions, like the relative humidity, can affect the activation properties of particles in the PSM (Kangasluoma *et al*. 2013, 2014). This would affect the determined particle concentration in each size bin and the size limits of each bin. We chose to use the calibration based on ammonium sulphate particles, which is an atmospherically relevant compound and can be generated in high purity and in high enough concentration in the desired sub-3 nm size range (Kangasluoma *et al*. 2013, 2014). There is evidence that ammonium sulphate activates much easier in diethylene glycol than e.g. organic compounds (Kangasluoma *et al*. 2014), and therefore we are likely to underestimate the concentration and size of particles in case of an organic aerosol. These issues in sub-3 nm size range needs to be addressed in the future. However, the changes in the particle

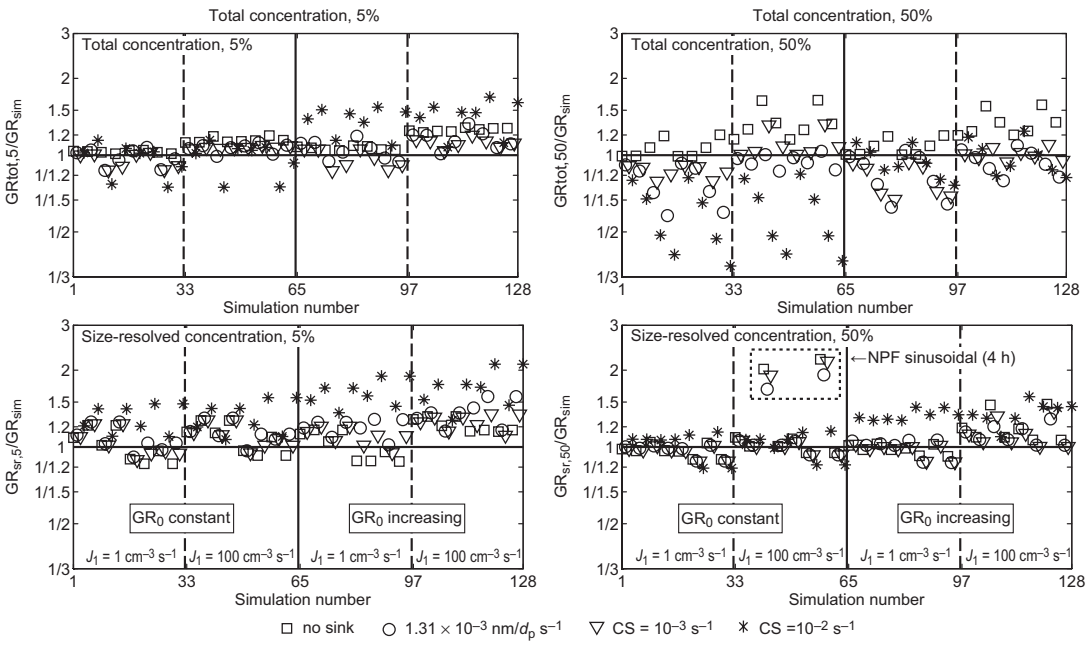

Fig. 16. The ratios of the growth rates determined with the appearance time method ($GR_{tot,5}$, $GR_{tot,50}$, $GR_{sr,5}$ and $GR_{sr,50}$) using the detection efficiency curves of Scenario 1 to the corresponding simulated growth rates. Each point corresponds to a single simulation with the simulation number on the *x*-axis. The type of the symbols denote the particle losses used in the simulation (*see* the legend). Points on the left (right) of the vertical, solid lines represent simulations with GR_0 being constant (increasing). Points on the left (right) of the vertical dashed lines represent simulations with J_1 = 1 cm^{-3} s^{-1} (J_1 = 100 cm^{-3} s^{-1}). The points inside the dotted rectangle correspond only to a part of the simulations with NPF following a sinusoidal path for 4 h. The ratios below (above) unity indicate that the method underestimated (overestimated) the simulated values.

activation efficiency due to composition can be also sometimes used for gaining knowledge of the particles, as in a CPC battery (Kulmala *et al*. 2007, Kangasluoma *et al*. 2014).

We showed using aerosol dynamic simulations and comparison with other instruments that the appearance time method used on the PSM data gives a good estimation of the particle growth rate in the size range 1–3 nm. The method is robust, at least if the shape of the particle size distribution is not heavily influenced by coagulation processes, especially coagulation scavenging. We also demonstrated that the growth rates are only slightly affected by possible errors in the determined PSM activation efficiency curves and that the methods are able to capture the diameter dependence of the growth rate. The most robust way of selecting the appearance time was either taking the time step when the total concentrations at different cut-off sizes reached 5% of their maximum value or when the size-resolved concentrations reached 50% of their maximum value. Comparing the two, the former was found to be more suitable for analyzing new particle formation events with long duration while the latter was less deluded by high coagulation sink.

As shown by Kuang *et al*. (2012b) the survival probability of particles into CCN sizes is clearly influenced by the initial GRs. The GRs are also used for scaling measured particle formation rates to the size of nucleating clusters (Kerminen and Kulmala, 2002). Therefore, using the correct GR for small particles is essential for estimating the effect of new particle formation on a larger scale. It has been already demonstrated that the PSM can give new valuable information about the aerosol formation process and particle concentration starting from the first molecular clusters (Kirkby *et al*. 2011, Kulmala *et al*. 2013), and especially when connected to ion and mass spectrometer data.

Acknowledgements: We would like to thank CERN for supporting CLOUD with important technical and financial resources, and for providing a particle beam from the CERN Proton Synchrotron. This research has received funding from the EC Seventh Framework Programme (Marie Curie Initial Training Network "CLOUD-ITN" grant no. 215072, ERC-Advanced "ATMNUCLE" grant (no. 227463) and the Academy of Finland Center of Excellence program (project no. 1118615), Academy of Finland project ComQuaCC: Computational research chain from quantum chemistry to climate change, project no. 135199, European Union Seventh Framework Programme (FP7/2007-2013) under grant agreement no. 262254, and the Eurostars Programme under contract no. E!6911 (GANS project).

References

Almeida J., Schobesberger S., Kürten A., Ortega I.K., Kupiainen-Määttä O., Praplan A.P., Adamov A., Amorim A.,Bianchi F., Breitenlechner M., David A., Dommen J., Donahue N.M., Downard A., Dunne E., Duplissy J., Ehrhart S., Flagan R.C., Franchin A., Guida R., Hakala J., Hansel A., Heinritzi M., Henschel H., Jokinen T., Junninen H., Kajos M., Kangasluoma J., Keskinen H., Kupc A., Kurtén T., Kvashin A.N., Laaksonen A., Lehtipalo K., Leiminger M., Leppä J., Loukonen V., Makhmutov V., McGrath M.J., Nieminen T., Olenius T., Onnela A., Petäjä T., Riccobono F., Riipinen I., Rissanen M., Rondo L., Ruuskanen T., Santos F.D., Sarnela N., Schallhart S., Schnitzhofer R., Seinfeld J.H., Simon M., Sipilä M., Stozhkov Y., Stratmann F., Tomé A., Tröstl J., Tsagkogeorgas G., Vaattovaara P., Viisainen Y., Virtanen A., Vrtala, A., Wagner P.E., Weingartner E., Wex H., Williamson C., Wimmer D., Ye P., Yli-Juuti T., Carslaw K.S., Kulmala M., Curtius J., Baltensperger U., Worsnop D.R., Vehkamäki H. & Kirkby J. 2013. Molecular understanding of sulphuric acid-amine particle nucleation in the atmosphere. *Nature* 502: 359–363.

Asmi E., Sipilä M., Manninen H., Vanhanen J., Lehtipalo K., Gagné S., Neitola K., Mirme A., Mirme S., Tamm E., Attoui M. & Kulmala M. 2009. Results of the first air ion spectrometer calibration and intercomparison workshop. *Atmos. Chem. Phys.* 9: 141–154.

Dal Maso M., Sogacheva L., Aalto P. P., Riipinen I., Komppula M., Tunved P., Korhonen L., Suur-Uski V., Hirsikko A., Kurtén T., Kerminen V.-M., Lihavainen H., Viisanen Y., Hansson H.C. & Kulmala M. 2007. Aerosol size distribution measurements at four Nordic field stations: identification, analysis and trajectory analysis of new particle formation bursts. *Tellus* 59B: 350–361.

Ehn M., Junninen H., Schobesberger S., Manninen H.E., Franchin A., Sipilä M., Petäjä T., Kerminen V.-M., Tammet H., Mirme A., Mirme S., Hõrrak U., Kulmala M. & Worsnop D.R. 2011. An instrumental comparison of mobility and mass measurements of atmospheric small ions. *Aerosol Sci. Technol.* 45: 522–532.

Flagan R.C. 1998. History of electrical aerosol measurements. *Aerosol Sci. Technol.* 28: 301–380.

Herrmann W., Eichler T., Bernardo N. & Fernández de la Mora, J. 2000. *Turbulent transition arises at Re 35 000 in a short Vienna-type DMA with a large laminarizing inlet*. Abstract to the annual conference of the AAAR, St. Louis, MO, 6–10 October 2000.

Hirsikko A., Laakso L., Hõrrak U., Aalto P.P., Kerminen V.-M. & Kulmala M. 2005. Annual and size dependent variation of growth rates and ion concentrations in boreal forest. *Boreal Env. Res.* 10: 357–369.

Hoppel W.A. & Frick G.M. 1986. Ion-aerosol attachment coefficients and the steady-state charge distribution on aerosol in a bipolar environment. *Aerosol Sci. Technol.* 5: 1–21.

Iida K., Stolzenburg M.R. & McMurry P.H. 2009. Effect of working fluid on sub-2nm particle detection with a laminar flow ultrafine condensation particle counter. *Aerosol Sci. Technol.* 43: 81–96.

Jiang J., Chen M., Kuang C., Attoui M. & McMurry P.H. 2011. Electrical mobility spectrometer using diethylene glycol condensation particle counter for measurement of aerosol size distributions down to 1 nm. *Aerosol Sci. Technol.* 45: 510–521.

Junninen H., Ehn M., Petäjä T., Luosujärvi L., Kotiaho T., Kostiainen R., Rohner U., Gonin M., Fuhrer K., Kulmala M. & Worsnop D.R. 2010. A high-resolution mass spectrometer to measure atmospheric ion composition. *Atmos. Meas. Tech.* 3: 1039–1053.

Kangasluoma J., Junninen H., Lehtipalo K. Mikkilä J., Vanhanen J., Attoui M., Sipilä M., Worsnop D., Kulmala M. & Petäjä T. 2013. Remarks on ion generation for CPC detection efficiency studies in sub 3 nm size range. *Aerosol Sci. Technol.* 5: 556–563.

Kangasluoma J., Kuang C., Wimmer D., Rissanen M. P., Lehtipalo K., Ehn M., Worsnop D.R., Wang J., Kulmala M. & Petäjä T. 2014. Sub-3 nm particle size and composition dependent response of a nano-CPC battery. *Atmos. Meas. Tech.* 7: 689–700.

Kerminen V.-M. & Kulmala M. 2002. Analytical formulae connecting the "real" and the "apparent" nucleation rate and the nuclei number concentration for atmospheric nucleation events. *J. Aerosol Sci.* 33: 609–622.

Kirkby J., Curtius J., Almeida J., Dunne E., Duplissy J., Erhart S., Franchin A., Gagné S., Ickes L., Kürten A., Kupc A., Metzger A., Riccobono F., Rondo L., Schobesberger S., Tsagkogeorgas G., Wimmer D., Amorim A., Bianchi F., Breitenlechner M., David A., Dommen J., Downard A., Ehn M., Flagan R.C., Haider S., Hansel A., Hauser D., Jud W., Junninen H., Kazil J., Kreissl F., Kvashin A., Laaksonen A., Lehtipalo K., Lima J., Lovejoy E.R., Makhmutov V., Mathot S., Mikkilä J., Minginette P., Mogo S., Nieminen T., Onnela A., Pereira P., Petäjä T., Schnitzhofer R., Seinfeld J.H., Sipilä M., Stozhkov Y., Stratmann F., Tome A., Vanhanen J., Viisanen Y., Vrtala A., Wagner, P.E. Walther H., Weingartner E., Wex H., Winkler P.M., Carslaw K.S., Worsnop D.R., Baltensperger U. & Kulmala M. 2011. The role of sulphuric acid, ammonia and galactic cosmic rays in atmospheric aerosol nucleation. *Nature* 476: 429–433.

Kuang C., Chen M., McMurry P.H. & Wang J. 2012a. Modification of Laminar flow ultrafine condensation particle

counters for the enhanced detection of 1 nm condensation nuclei. *Aerosol Sci. Technol.* 46: 309–315.

Kuang C., Chen M., Zhao J., Smith J., McMurry P.H. & Wang J. 2012b. Size and time-resolved growth rate measurements of 1 to 5 nm freshly formed atmospheric nuclei. *Atmos. Chem. Phys.* 12: 3573–3589.

Kulmala M., Vehkamäki H., Petäjä T., Dal Maso M., Lauri A., Kerminen V.-M., Birmili W. & McMurry P.H. 2004. Formation and growth rates of ultrafine atmospheric particles: a review of observations. *J. Aerosol Sci.* 35: 143–176.

Kulmala M., Petäjä T., Nieminen T., Sipilä M., Manninen H.E., Lehtipalo K., Dal Maso M., Aalto P.P, Junninen H., Paasonen P., Riipinen I., Lehtinen K.E.J., Laaksonen, A. & Kerminen V.-M. 2012. Measurement of the nucleation of atmospheric aerosol particles. *Nature Protocols* 7: 1651–1667.

Kulmala M., Mordas G., Petäjä T., Grönholm T., Aalto P.P., Vehkamäki H., Hienola A. I., Herrmann E., Sipilä M., Riipinen I., Manninen H.E., Hämeri K., Stratmann F., Bilde M., Winkler P.M., Birmili W. & Wagner P.E. 2007. The condensation particle counter battery (CPCB): A new tool to investigate the activation properties of nanoparticles. *J. Aerosol Sci.* 38: 289–304.

Kulmala M., Kontkanen J., Junninen H., Lehtipalo K., Manninen H.E., Nieminen T., Petäjä T., Sipilä M., Schobesberger S., Rantala P., Franchin A., Jokinen T., Järvinen E., Äijälä M., Kangasluoma J., Hakala J., Aalto P.P, Paasonen P., Mikkilä J., Vanhanen J., Aalto J., Hakola H., Makkonen U., Ruuskanen T., Mauldin R.L.III, Duplissy J., Vehkamäki H., Bäck J., Kortelainen A., Riipinen I., Kúrten T., Johnston M.V. Smith J.N., Ehn M., Mentel T.F., Lehtinen K.E.J., Laaksonen A., Kerminen V.-M. & Worsnop D. 2013. Direct observations of atmospheric aerosol nucleation. *Science* 22: 911–912.

Lehtipalo K., Sipilä M., Riipinen I., Nieminen T. & Kulmala M. 2009. Analysis of atmospheric neutral and charged molecular clusters in boreal forest using pulse-height CPC. *Atmos. Chem. Phys.* 9: 4177–4184.

Lehtipalo K., Kulmala M., Sipilä M., Petäjä T., Vana M., Ceburnis D., Dupuy R. & O'Dowd C. 2010. Nanoparticles in boreal forest and coastal environment: a comparison of observations and implications of the nucleation mechanism. *Atmos. Chem. Phys.* 10: 7009–7016.

Leppä J., Anttila T., Kerminen V.-M., Kulmala M. & Lehtinen K.E.J. 2011. Atmospheric new particle formation: real and apparent growth of neutral and charged particles. *Atmos. Chem. Phys.* 11: 4939–4955.

Leppä J., Gagné S., Laakso L., Manninen H.E., Lehtinen K.E.J., Kulmala M. & Kerminen V.-M. 2013. Using measurements of the aerosol charging state in determination of the particle growth rate and the proportion of ion-induced nucleation. *Atmos. Chem. Phys.* 13: 463–486.

Leppä J., Kerminen V.-M., Laakso L., Korhonen H., Lehtinen K.E.J., Gagné S., Manninen H.E., Nieminen T. & Kulmala M. 2009. Ion-UHMA: a model for simulating the dynamics of neutral and charged aerosol particles. *Boreal Env. Res.* 14: 559–575.

Lähde T., Rönkkö T., Virtanen A., Schuck T.J., Pirjola L., Hämeri K., Kulmala M., Arnold F., Rothe D. & Keskinen, J. 2009. Heavy duty diesel engine exhaust aerosol particle and ion measurements. *Environ. Sci. Technol.* 43: 163–168.

Manninen H.E., Nieminen T., Riipinen I., Yli-Juuti T., Gagné S., Asmi E., Aalto P.P., Petäjä T., Kerminen V.-M. & Kulmala M. 2009. Charged and total particle formation and growth rates during EUCAARI 2007 campaign in Hyytiälä. *Atmos. Chem. Phys.* 9: 4077–4089.

Manninen H.E., Nieminen T., Asmi E., Gagné S., Häkkinen S., Lehtipalo K., Aalto P., Vana M., Mirme A., Mirme S., Hörrak U., Plass-Dülmer C., Stange G., Kiss G., Hoffer A., Törő N., Moerman M., Henzing B., de Leeuw G., Brinkenberg M., Kouvarakis G. N., Bougiatioti A., Mihalopoulos N., O'Dowd C., Ceburnis D., Arneth A., Svenningsson B., Swietlicki E., Tarozzi L., Decesari S., Facchini M. C., Birmili W., Sonntag A., Wiedensohler A., Boulon J., Sellegri K., Laj P., Gysel M., Bukowiecki N., Weingartner E., Wehrle G., Laaksonen A., Hamed A., Joutsensaari J., Petäjä T., Kerminen V.-M. & Kulmala M. 2010. EUCAARI ion spectrometer measurements at 12 European sites — analysis of new particle formation events. *Atmos. Chem. Phys.* 10: 7907–7927.

Mirme A., Tamm E., Mordas G., Vana M., Uin J., Mirme S., Bernotas T., Laakso L., Hirsikko A. & Kulmala M. 2007. A wide-range multi-channel Air Ion Spectrometer. *Boreal Env. Res.* 12: 247–264.

Nadykto A.B. & Yu F. 2003. Uptake of neutral polar vapor molecules by charged clusters/particles: Enhancement due to dipole-charge interaction. *J. Geophys. Res.* 108: 4717, doi:10.1029/2003JD003664.

Riccobono F., Rondo L., Sipilä M., Barmet P., Curtius J., Dommen J., Ehn M., Ehrhart S., Kulmala M., Kürten A., Mikkilä J., Paasonen P., Petäjä T., Weingartner E. & Baltensperger U. 2012. Contribution of sulfuric acid and oxidized organic compounds to particle formation and growth. *Atmos. Chem. Phys.* 12: 9427–9439.

Schobesberger S., Junninen H., Bianchi F., Lönn G., Ehn M., Lehtipalo K., Dommen J., Ehrhart S., Ortega I.K., Franchin A., Nieminen T., Riccobono F., Hutterli M., Duplissy J., Almeida J., Amorim A., Breitenlechner M., Downard A.J., Dunne E.M., Flagan R.C., Kajos M., Keskinen H., Kirkby J., Kupc A., Kürten A., Kurtén T., Laaksonen A., Mathot S., Onnela A., Praplan A.P., Rondo L., Santos F.D., Schallhart S., Schnitzhofer R., Sipilä M., Tomé A., Tsagkogeorgas G., Vehkamäki H., Wimmer D., Baltensperger U., Carslaw K.S., Curtius J., Hansel A., Petäjä T., Kulmala M., Donahue N.M. & Worsnop D.R. 2013. Molecular understanding of atmospheric particle formation from sulfuric acid and large oxidized organic molecules. *Proc. Natl. Acad. Sci. USA* 110: 17223–17228.

Sihto S.-L., Kulmala M., Kerminen V.-M., Dal Maso M., Petäjä T., Riipinen I., Korhonen H., Arnold F., Janson R., Boy M., Laaksonen A. & Lehtinen K.E.J. 2006. Atmospheric sulphuric acid and aerosol formation: implications from atmospheric measurements for nucleation and early growth mechanisms. *Atmos. Chem. Phys.* 6: 4079–4091.

Sipilä M., Lehtipalo K., Attoui M., Neitola K., Petäjä T., Aalto P.P., O'Dowd C.D. & Kulmala M. 2009. Labora-

tory verification of PH-CPC's ability to monitor atmospheric sub-3 nm clusters. *Aerosol Sci. Technol.* 43, 126–135.

Sipilä M., Lehtipalo K., Kulmala M., Petäjä T., Junninen H, Aalto P.P, Manninen H.E., Vartiainen E., Riipinen I., Kyrö E.-M., Curtius J., Kürten A., Borrmann S. & O'Dowd C.D. 2008. Applicability of condensation particle counters to measure atmospheric clusters. *Atmos. Chem. Phys.* 8: 4049–4060.

Steiner G. & Reischl G.P. 2012. The effect of carrier gas contaminants on the charging probability of aerosols under bipolar charging conditions. *J. Aerosol Sci.* 54: 21–31.

Tammet H. 2006. Continuous scanning of the mobility and size distribution of charged clusters and nanoparticles in atmospheric air and the Balanced Scanning Mobility Analyzer BSMA. *Atmos. Res.* 82: 523–535.

Ude S. & Fernández de la Mora J. 2005. Molecular monodisperse mobility and mass standards from electrosprays of tetra-alkyl ammonium halides. *J. Aerosol Sci.* 36: 1224–1237.

Vanhanen J., Mikkilä J., Lehtipalo K., Sipilä M., Manninen H.E., Siivola E., Petäjä T. & Kulmala M. 2011. Particle Size Magnifier for nano-CN detection. *Aerosol Sci. Technol.* 45: 533–542.

Wiedensohler A. 1988. An approximation of the bipolar charge distribution for particles in the submicron size Range. *J. Aerosol Sci.* 19: 387–389.

Wiedensohler A., Birmili W., Nowak A., Sonntag A., Weinhold K., Merkel M., Wehner B., Tuch T., Pfeifer S., Fiebig M., Fjäraa A.M., Asmi E., Sellegri K., Depuy R., Venzac H., Villani P., Laj P., Aalto P., Ogren J. A., Swietlicki E., Williams P., Roldin P., Quincey P., Hüglin C., Fierz-Schmidhauser R., Gysel M., Weingartner E., Riccobono F., Santos S., Grüning C., Faloon K., Beddows D., Harrison R., Monahan C., Jennings S.G., O'Dowd C.D., Marinoni A., Horn H.-G., Keck L., Jiang J., Scheckman J., McMurry P.H., Deng Z., Zhao C.S., Moerman M., Henzing B., de Leeuw G., Löschau G. & Bastian S. 2012. Mobility particle size spectrometers: harmonization of technical standards and data structure to facilitate high quality long-term observations of atmospheric particle number size distributions. *Atmos. Meas. Tech.* 5: 657–685.

Wimmer D., Lehtipalo K., Franchin A., Kangasluoma J., Kreissl F., Kürten A., Kupc A., Metzger A., Mikkilä J., Petäjä T., Riccobono F., Vanhanen J., Kulmala M. & Curtius J. 2013. Performance of diethylene glycol-based particle counters in the sub-3 nm size range. *Atmos. Meas. Tech.* 6: 1793–1804.

Yli-Juuti T., Nieminen T., Hirsikko A., Aalto P.P., Asmi E., Hõrrak U., Manninen H.E., Patokoski J., Dal Maso M., Petäjä T., Rinne J., Kulmala M. & Riipinen I. 2011. Growth rates of nucleation mode particles in Hyytiälä during 2003–2009: variation with particle size, season, data analysis method and ambient conditions. *Atmos. Chem. Phys.* 11: 12865–12886.

Zhao J., Smith J.N., Eisele F.L., Chen M., Kuang C. & McMurry P.H. 2011. Observations of neutral sulphuric acid-amine containing clusters in laboratory and ambient measurements. *Atmos. Chem. Phys.* 11: 10823–10836.